ACS APPLIED MATERIALS & INTERFACES

Research Article

www.acsami.org

Maghemite Nanoparticles on Electrospun CNFs Template as Prospective Lithium-Ion Battery Anode

Yongzhi Wu,[†,‡,§] Peining Zhu,[§] M. V. Reddy,*[,‡] B. V. R. Chowdari,[‡] and S. Ramakrishna[§]

[†]NUS Graduate School for Integrative Sciences and Engineering, National University of Singapore (NUS), Singapore 119260

[‡]Department of Physics, National University of Singapore (NUS), Singapore 117542

[§]Department of Mechanical Engineering, Center for Nanofibers & Nanotechnology, NUS Nanoscience and Nanotechnology Initiative, National University of Singapore (NUS), Singapore 117581

Supporting Information

ABSTRACT: In this work, maghemite (γ-Fe_2O_3) nanoparticles were uniformly coated on carbon nanofibers (CNFs) by a hybrid synthesis procedure combining an electrospinning technique and hydrothermal method. Polyacrylonitrile nanofibers fabricated by the electrospinning technique serve as a robust support for iron oxide precursors during the hydrothermal process and successfully limit the aggregation of nanoparticles at the following carbonization step. The best materials were optimized under a carbonization condition of 600 °C for 12 h. X-ray diffraction and electron microscopy studies confirm the formation of a maghemite structure standing on the surface of CNFs. The average size of γ-Fe_2O_3 nanoparticles is below 100 nm, whereas CNFs are ~150 nm in diameter. In comparison with aggregated bare iron oxide nanoparticles, the as-prepared carbon−maghemite nanofibers exhibit a higher surface area and greatly improved electrochemical performance (>830 mAh g^{-1} at 50 mA g^{-1} for 40 cycles and high rate capacity up to 5 A g^{-1} in the voltage range of 0.005−3 V vs Li). The greatly enhanced electrochemical performance is attributed to the unique one-dimensional nanostructure and the limited aggregation of nanoparticles.

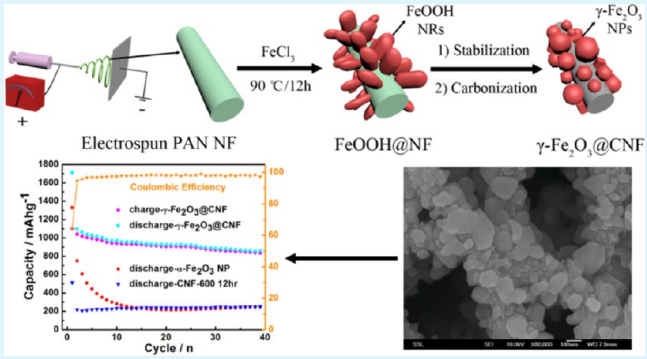

KEYWORDS: *electrospun CNF, maghemite nanoparticles, lithium-ion battery, anode material*

INTRODUCTION

With the increasing energy demand from the accelerating global economy, renewable energy sources have become more and more favorable. The rechargeable lithium-ion battery (LIB) is one of such circumvents to achieve sustainability, self-maintenance, low carbon emission, and high efficiency[1] tackling the future economic issues. Although great efforts have been invested and many exciting findings have been reported along the development of LIBs in the past two decades, current LIBs are delivering a moderate practical capacity far from that of high-energy lithium metal (3860 mAh g^{-1}), which hinders their application for hybrid electric vehicles (HEVs) and plug-in hybrid electric vehicles (PHEVs).[1−5] Currently, most commercial LIBs use graphite and other carbon materials as anode, delivering a maximum theoretical capacity of 372 mAh g^{-1} as LiC_6 compounds formed during lithiation limit the high-energy storage for carbon.[6] Thus, many alternative materials with higher capacities, including silicon (Si), tin (Sn), and transitional metal oxide-based materials, have been extensively studied to replace graphite.[7] However, such high-energy materials generally suffer from capacity fading due to large volume expansion and low rate capacity caused by their poor electronic conductivity.

To solve the above problems, anode materials with a one-dimensional (1D) nanostructure have been extensively studied as they can be better at relieving mechanical stress during volumetric changes and enhancing the overall conductivity.[4,8] Recently, 1D carbon nanofibers (CNFs) have demonstrated their superiority of achieving high-rate electrochemical performance for real LIB application due to enhanced electronic conductivity, well-sustained nanomorphology during cycling, and free-standing characteristic.[9−12] The simplest method to fabricate CNFs at a scalable rate is by the electrospinning technique and subsequent thermal treatment, where the nanofiber diameter and direction can be controlled by applying different settings.[13,14] However, the energy density delivered by bare electrospun CNFs is limited in terms of the amount of lithium possible to be inserted and voltage hysteresis between the charge/discharge process;[15] therefore, further optimization in fabrication methods or other derivative morphology (hollow CNFs[16]) development are conducted to enhance the overall capacity for electrospun CNFs. To further

Received: November 8, 2013
Accepted: January 2, 2014
Published: January 2, 2014

increase the lithium accommodation in electrospun CNFs, various metal oxide-based materials of high capacity, including SnO_2,[12] α-Fe_2O_3,[17] and NiO/RuO_2,[18] and also for supercapacitor studies[19] have been combined via direct electrospinning polymeric solution with precursor salts. They all demonstrate improved capacity than bare electrospun CNFs or commercial graphite anodes. However, such a direct electrospinning technique limits the loading amount of active materials, which lowers the overall capacity that can be achieved as anode material.

Herein, we exhibit a hybrid synthesis procedure combining the electrospinning technique and hydrothermal method to fabricate γ-Fe_2O_3 nanoparticles (NP)@CNF as a high-performance anode material for LIB. The procedure introduced here is able to increase the γ-Fe_2O_3 loading up to more than 60%, which leads to a high reversible capacity > 830 mAh g^{-1} for 40 cycles. The material can also survive high current charge–discharge up to 5 A g^{-1} with the support of electrospun CNFs. Interestingly, the phase of iron oxides standing on CNF nanocomposites prepared at high temperature are maghemite (γ-Fe_2O_3) rather than hematite (α-Fe_2O_3). To our knowledge, this is the first report of detailed structural and electrochemical studies on γ-Fe_2O_3 based CNF nanocomposites.

EXPERIMENTAL SECTION

Hybrid Synthesis of γ-Fe_2O_3 NP@CNF. Poly(acrylonitrile) (PAN) (M_w ~ 150 000, 99%), *N*,*N*-dimethylformamide (DMF, 99%), and $FeCl_3$ (97%) were purchased and used as received from Sigma-Aldrich. An 8 wt % DMF solution of PAN was prepared and vigorously stirred for at least 2 h to obtain homogeneous dispersion. PAN nanofibers were collected on the alumina foil 12 cm away from a syringe needle linked to a variable high voltage power supply of 18 kV with a feeding rate of 0.8 mL/h. Then, FeOOH nanorods were synthesized on the surface of PAN nanofibers via a hydrothermal process as reported elsewhere.[20] Briefly, 0.243 g of $FeCl_3$ was dissolved in 30 mL of deionized (DI) water under magnetic stirring for 4 h. Then the resulting solution was transferred into a 50 mL Teflon-lined autoclave with electrospun PAN nanofibers. The autoclave was sealed and heated at 90 °C for 12 h, and cooled to room temperature. The membrane was then collected out, sonicated for 10 min in DI water, washed for at least three times to eliminate isolated FeOOH nanorods, and dried at 70 °C for 12 h. The as-obtained membrane was first stabilized in an ambient atmosphere at 280 °C for 2 h and then carbonized under argon protection at 600 °C for 12 h. For comparison, iron oxide nanoparticles were also prepared via direct calcination of the as-obtained membrane in air at 600 °C for 12 h. Different carbonization conditions were also tried at 600 °C for 2 h and 800 °C for 12 h, respectively, to make a comparative study.

Characterization. The obtained samples characterized using X-ray powder diffraction (XRD, Philips X'PERT PANalytical) with Cu Kα radiation. The microstructure and morphology of the samples were recorded using a scanning electron microscope (SEM, JEOL JSM-6700F) and a high-resolution transmission electron microscope (HR-TEM, JEOL-JEM 3010). Thermogravimetric analysis (TGA) was conducted with a TA Instruments 2960. The Brunauer–Emmett–Teller (BET) surface areas were determined by using a Micromeritics (TriStar, USA). Further details on instrumentation are given in our previous study.[21]

Electrochemical Evaluation of γ-Fe_2O_3 NP@CNF. As for typical electrochemical studies,[18,22] the as-prepared γ-Fe_2O_3 NP@CNF was milled and mixed with super carbon black and binder (polyvinylidene difluoride, PVdF) in the weight ratio of 70:15:15 using *N*-methyl pyrrolidone (NMP) as dissolving solvent. The mixture was stirred overnight to form a homogeneous slurry, which was further spread on an etched copper foil (thickness, 15 μm; Shenzhen Vanlead Tech. Co. Ltd., China) as current collector by using a doctor-blade technique. The copper foil was then dried at 80 °C under vacuum and cut into circular disks (16 mm in diameter) to serve as testing electrodes. Lithium metal foil (Kyokuto Metal Co., Japan) as counter electrode, 1 M $LiPF_6$ in ethylene carbonate (EC) and diethyl carbonate (DEC) (1:1 in volume) (Merck) as electrolyte, and a Celgard 2502 membrane as separator were assembled together with testing electrodes to obtain a 2016-type coin cell in an argon-filled glovebox (MBraun, Germany). Before all electrochemical measurement, cells were aged for 12 h and then tested for cyclic voltammetry (CV) measurement, galvanostatic cycling, and rate capacity studies; they were performed between 0.005 and 3 V vs Li/Li^+ using a computer controlled by an Arbin Battery tester (US, BT-2043). Rate capability studies were also conducted ranging from 0.1 to 5 A g^{-1}.

RESULT AND DISCUSSION

Figure 1 demonstrates the schematic illustration of the synthesis process for γ-Fe_2O_3 NP@CNF and corresponding

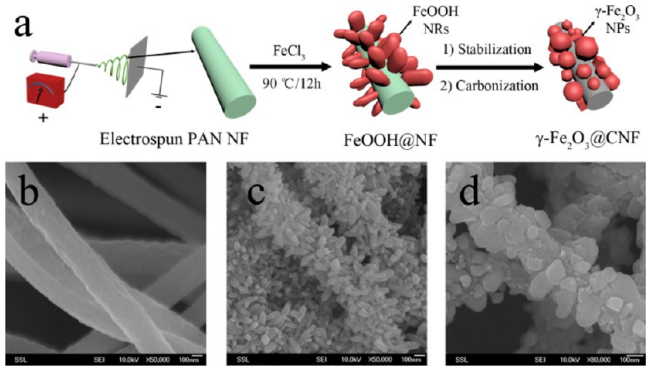

Figure 1. (a) Schematic illustration of the electrospinning process and synthesis of the γ-Fe_2O_3 NP@CNF. (b–d) SEM images of the bare electrospun PAN NF, FeOOH NR@NF, and γ-Fe_2O_3 NP@CNF, respectively.

SEM images. Using the electrospinning technique, bare PAN nanofibers (NFs) could be obtained with diameters ranging from 150 to 250 nm, as demonstrated in Figure 1b in the first step. The surface of electrospun PAN NFs was coated with a layer of FeOOH nanorods (NRs) via a hydrothermal process in aqueous $FeCl_3$ solution similar to previous reports.[23,24] The average diameter and length of the FeOOH NRs attached on PAN NFs synthesized at 90 °C are 60 ± 5 nm and ~200 nm, respectively, as could be observed in Figure 1c. The aspect ratio (~3) obtained is much lower than that of other bare FeOOH NRs prepared with the assistance of a template surfactant (~13)[23] or in a direct hydrothermal way (~25).[24] Therefore, the result indicates that electrospun PAN NFs can not only serve as an organic scaffold for the ease of FeOOH NRs' formation but also prohibit the excessive growth of FeOOH NRs along their length axis. Afterward, the FeOOH NRs@electrospun PAN NFs underwent the standard two steps of producing CNFs:[9] (1) stabilization in air and (2) carbonization under the protection of inert gas. Here, different carbonization conditions (600 °C for 12 h, 600 °C for 2 h, and 800 °C for 12 h under Ar protection) have been studied to make the comparison for morphology of the final products, as well as their electrochemical performance.

As demonstrated in Figure 1d, the morphology of FeOOH NRs attached on NFs transferred to nanoparticles (NPs) after the carbonization process at 600 °C for 12 h in Ar gas. The size and distribution of iron oxide NPs (shown in Figure 2a) are well controlled on the reserved nanostructure of CNFs in comparison with the morphology obtained from carbonization

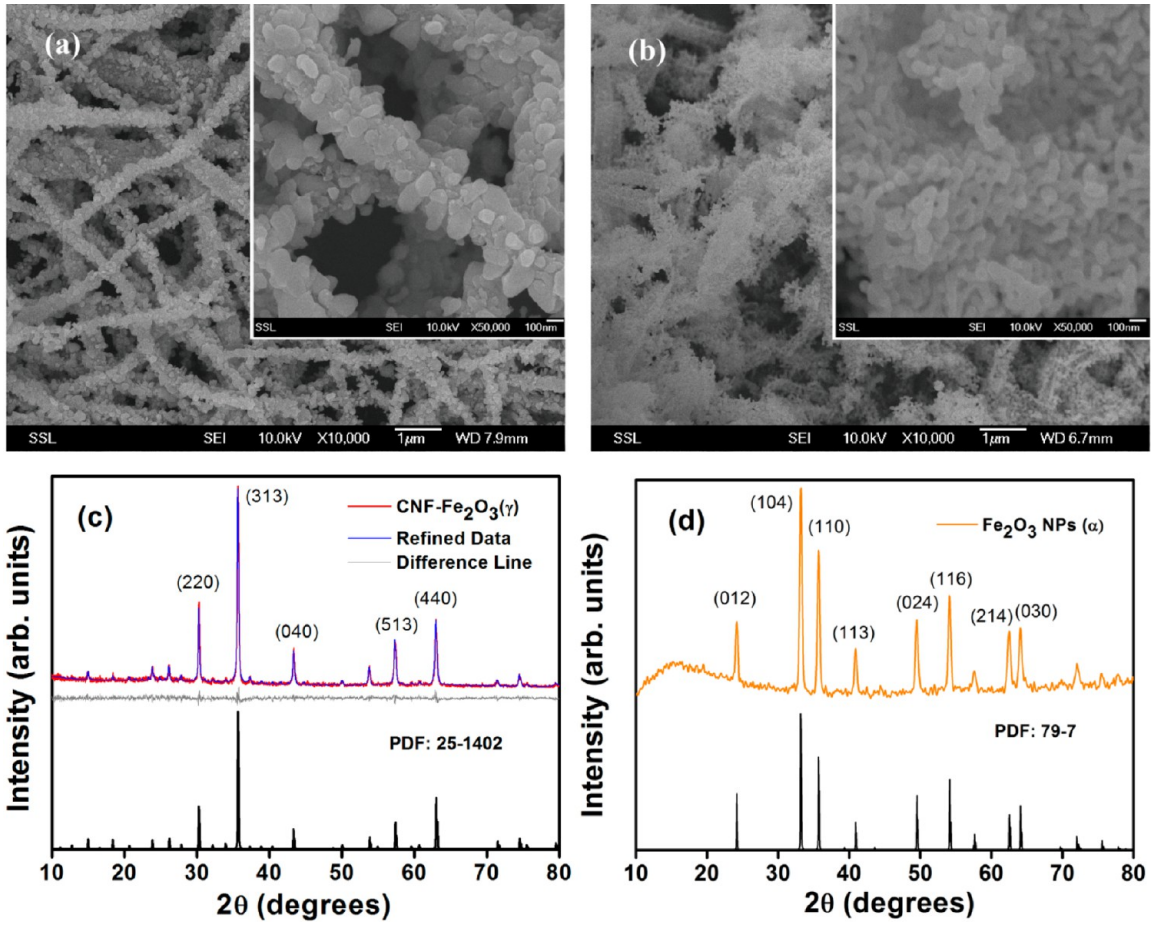

Figure 2. Morphological characterization of (a) the as-synthesized γ-Fe_2O_3 NP@CNF (600 °C for 12 h), the inset is high-magnification; and (b) the directly synthesized bare α-Fe_2O_3 NP, the inset is high-magnification. (c) XRD pattern of the as-synthesized γ-Fe_2O_3 NP@CNF (600 °C for 12 h) with fitted data achieved by Rietveld refinement. (d) XRD pattern of the directly synthesized bare α-Fe_2O_3 NP.

at 600 °C for 2 h and 800 °C for 12 h (Figure S1, Supporting Information). Under the condition that the calcination time was shortened to 2 h at 600 °C, iron oxide nanoparticles on CNFs were less developed. On the other hand, if the calcination temperature increased to 800 °C at a prolonged period of 12 h, iron oxide nanoparticles would grow up to hundreds of nanometers, thus deteriorating the overall fiberous morphology. As shown in Figure 2c and the Supporting Information (Figure S2), the corresponding XRD patterns of iron oxide on electrospun CNF indicate that all the diffraction peaks can be assigned to tetragonal structured maghemite (γ-Fe_2O_3). As the sample obtained after carbonization at 600 °C for 12 h demonstrates the best morphology and clearest XRD pattern, it would be fair to make it representative in the later discussion on γ-Fe_2O_3@CNF. The crystal structure of γ-Fe_2O_3@CNF has been confirmed using the Rietveld method implemented in TOPAS software version 2.1 (Figure 2c). The structure calculated from the XRD pattern, with lattice parameters a = 8.3482(5) Å, c = 25.0169(3) Å in space group $P4_32_12$, matches very well with JCPDS card no. 25-1402. The average crystallize size is 61.3 nm, which is consistent with particles observed in high-magnification SEM (Figure 2a, inset). In contrast with γ-Fe_2O_3 NPs standing on CNFs, bare Fe_2O_3 prepared via direct calcination in air at 600 °C for 12 h is presenting an α phase according to its XRD pattern, in good agreement with JCPDS card no. 79-7 (Figure 2d). Its morphology shown in Figure 2b turns out to be aggregated nanoparticles in the size on a micrometer scale. The phase difference between γ-Fe_2O_3@CNF and bare Fe_2O_3 might be due to the reduction effect of CNFs, which has already been noted when electrospun CNFs were integrated with other metal oxides.[18,25] As demonstrated by the above results, the 1D nanostructure is capable of preventing small nanoparticles to aggregate into large granules during the hydrothermal process. This is consistent with the findings in the previous study.[22] Furthermore, electrospun CNFs also demonstrate their reduction effect that helps to produce the γ-Fe_2O_3 phase, which is more stable due to the thermodynamic considerations at nanosize.[26] On the other hand, γ-Fe_2O_3@CNF derived from co-decomposition of PAN nanofiber/iron precursors also takes the advantages of robust and conductive CNF's structures prepared at low carbonization temperature.[27−29]

Figure 3 shows the morphological characterization of γ-Fe_2O_3 NP@CNF using TEM photographs. The low-resolution (LR) TEM image in Figure 3a presents a clear view of γ-Fe_2O_3 NPs standing on the CNF 1D nanostructure. The sizes of γ-Fe_2O_3 NPs range from 50 to 70 nm, further verifying the average size value calculated from the XRD pattern by Rietveld refinement. From the HRTEM image (shown in Figure 3b), lattice fringes for the d-spacing of 2.53 Å corresponding to the most intensive peak at (313) in the XRD pattern can be clearly observed. The inset of Figure 3b is also in good agreement with the above TEM and XRD results. The measurements carried out in this work confirm the structure and phase of maghemite

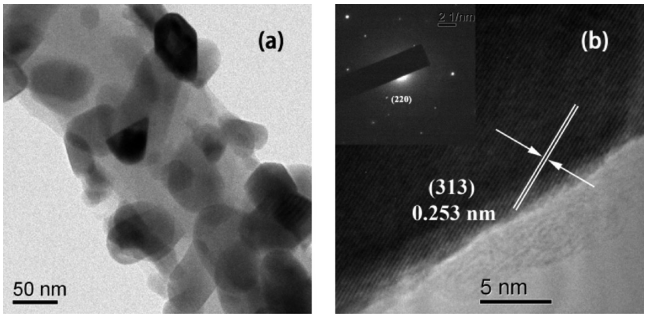

Figure 3. TEM images of the as-synthesized γ-Fe_2O_3@CNF: (a) LRTEM; (b) HRTEM image presenting clear lattice fringes at the (119) peak; inset: selected area electron diffraction (SAED) pattern.

nanoparticles coated on CNFs synthesized by our strategy combing the electrospinning technique and hydrothermal method.

The carbon content of γ-Fe_2O_3@CNF is significant for improved lithium storage performance as high capacity is determined by iron oxide while high power relies on CNF content. Herein, TGA was performed to analyze the CNF content present in γ-Fe_2O_3@CNF nanocomposites. As can be seen in Figure 4a, the early weight loss until 200 °C of the as-synthesized γ-Fe_2O_3@CNF is probably due to the removal of surface hydroxyl groups and/or surface absorbed water. Noticeably, this early loss is minimal (~4.1%) and its impact would be lessened as electrode materials since it would take serious procedures to eliminate moisture for LIB electrode fabrication. As the weight variation for bare γ-Fe_2O_3 is considerably small till 900 °C,[30] the weight loss between 300 and 500 °C can be mainly attributed to the oxidation of central CNFs. Thus, the carbon content of γ-Fe_2O_3@CNF can be determined to be ~35.7% by weight. On the contrary, the mass loading of active materials on electrospun CNFs is ~60.2%, which is much higher than that achieved via direct calcination of PAN nanofibers together with metal salts.[17] The high mass loading of active materials is helpful to achieve high reversible capacity as an anode in LIBs. The surface area-to-volume ratios of γ-Fe_2O_3@CNF and α-Fe_2O_3 NP were measured by BET analysis are shown in Figure 4b. The BET surface areas calculated for these two counterparts are ~18.3 and 6.6 $m^2\ g^{-1}$, respectively. The larger surface area of γ-Fe_2O_3@CNF once more confirms its well-controlled aggregation of iron oxide nanoparticles on the 1D CNF, which can facilitate faster electronic conduction and provide more accommodation sites for lithium ions. As expected, γ-Fe_2O_3@CNF fabricated under other carbonization conditions has a smaller surface area (600 °C for 2 h: 12.6 $m^2\ g^{-1}$; 800 °C for 12 h: 7.9 $m^2\ g^{-1}$) due to the morphological defects described above. Motivated by the well-controlled structure and composition of γ-Fe_2O_3@CNF, the electrochemical performance was examined as an anode material in LIB applications.

The electrochemical reaction of Li with Fe_2O_3 and CNF can be described in the following eqs 1−4,[11,27,31−34] respectively:

$$Fe_2O_3 + xLi^+ + xe^- \rightarrow Li_xFe_2O_3\ (x \leq 2) \quad (1)$$

$$Li_2Fe_2O_3 + 4Li^+ + 4e^- \rightarrow 2Fe + 3Li_2O \quad (2)$$

$$2Fe + 3Li_2O \leftrightarrow Fe_2O_3 + 6Li^+ + 6e^- \quad (3)$$

$$C_6 + Li^+ + e^- \leftrightarrow LiC_6 \quad (4)$$

In the first cycle, γ-Fe_2O_3 underwent irreversible reactions according to eqs 1 and 2. This was confirmed by the three cathodic peaks observed at 1.21, 0.91, and 0.72 V as demonstrated in the cyclic voltammgrams (CVs) of γ-Fe_2O_3@CNF in the potential window of 0.005−3 V at the scan rate of 58 $\mu V\ s^{-1}$ (Figure 5). The moles of Li uptake per γ-Fe_2O_3@CNF during the initial reaction can be obtained using the galvanostatic cycling profile shown in Figure 6a. First, the cell was discharged from the open-circuit voltage (OCV = 2.54 V) toward 0.005 V. Corresponding to the first cathodic peak at

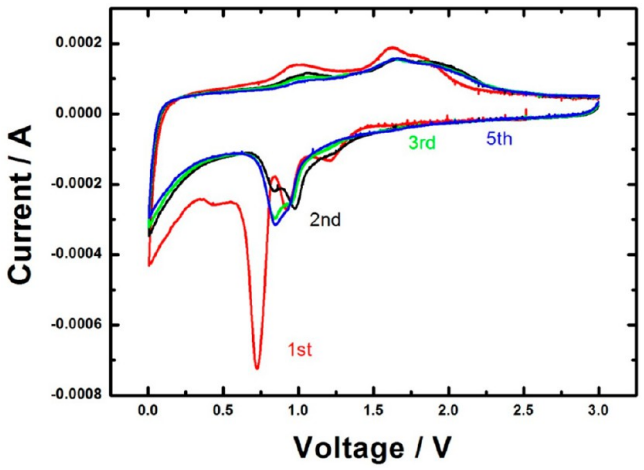

Figure 5. Cyclic voltammograms of γ-Fe_2O_3@CNF. Potential window: 0.005−3 V; scan rate: 58 $\mu V\ s^{-1}$. Li metal was used as the counter and reference electrodes.

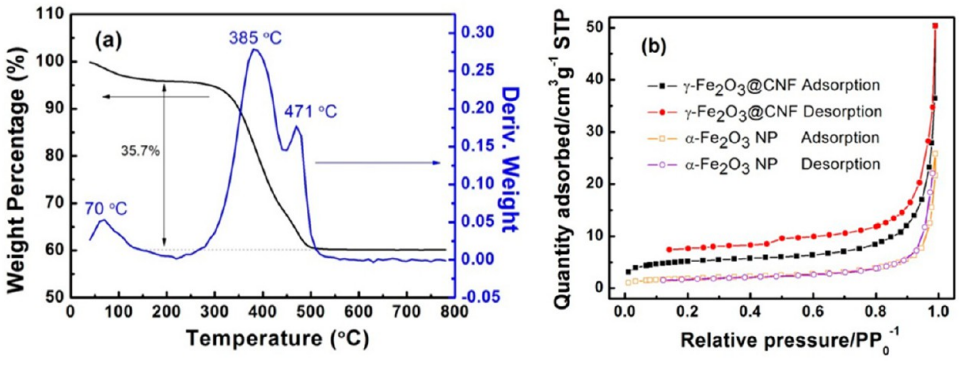

Figure 4. (a) TGA analysis of γ-Fe_2O_3 NP@CNF. (b) BET analysis of γ-Fe_2O_3@CNF in comparison with α-Fe_2O_3 NP.

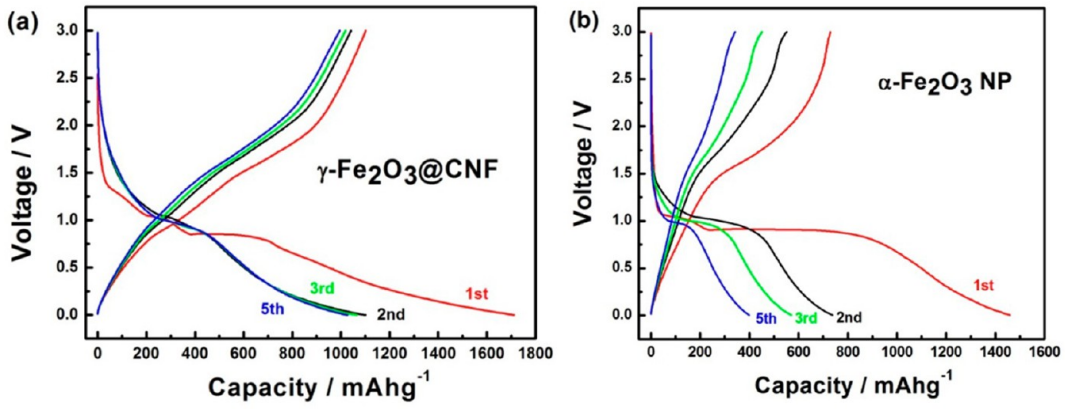

Figure 6. Galvanostatic profiles of the electrodes made from (a) γ-Fe_2O_3@CNF and (b) α-Fe_2O_3 NP over the voltage range of 0.005−3.0 V measured for the 1st, 2nd, 3rd, and 5th cycles at a current density of 50 mA g^{-1}.

1.21 V, a small amount of lithium (~186 mAh g^{-1}, eq 1) could be inserted into the crystal structure of γ-Fe_2O_3. The voltage of the cell steeply dropped to 1.06 V in this reaction. In the next step, a small plateau could be observed at 1.06 V and the voltage slowly dropped down to 0.85 V, corresponding to the second cathodic peak at 0.91 V. The capacity correlated to the voltage drop reached 370 mAh g^{-1} equivalent to the uptake of 2.2 mol of Li (x = 2, in eq 1; the additional 0.2 Li uptake could be assigned to the contribution of CNF substrate). The formation of $Li_xFe_2O_3$ ($x \leq 2$) in the above steps demonstrated no crystal structure destruction. Upon further discharge, a much longer voltage plateau at 0.85 V could be seen. Discharging from the OCV to the end of this plateau, a capacity of 700 mAh g^{-1} could be achieved, representing a total uptake of 4.2 Li per mole of γ-Fe_2O_3@CNF due to the complete reduction of Fe^{3+} to Fe^0 and the evolution of the Li_2O matrix (eq 2). The high intensity peak at 0.72 V corresponded to the decomposition of $Li_xFe_2O_3$, the crystal structure destruction during this reduction process, and the decomposition of electrolyte.[7] The electrolyte began to be reduced gradually below 0.8 V vs Li^+/Li[35] and form a solid electrolyte interface (SEI) layer, which is consistent with the long, sloping profile starting from 0.85 V. The total discharge capacity in the first cycle finally reached 1710 (±10) mAh g^{-1} until the lower voltage cutoff at 0.005 V, more than half of which came from voltage below 0.85 V. The relatively ultralarge capacity obtained in this region can be originated from SEI formation, further lithium storage via interfacial reaction at the metal/Li_2O phase boundary,[7,36−39] and also the formation of polymeric species deposited on metal oxide anodes at low potential.[40,41] It should also be noted that the 1D nanostructure introduced by CNFs provides additional surface area for the contact between electrolyte and active materials, which would increase Li consumption during initial discharge. Moreover, CNFs can also accommodate Li ions during cycling similar to graphite (eq 4). It could be observed that, in the first discharge, the fourth cathodic peak was broad around 0.42 V, assigned to the reaction of Li with CNFs. The peak position is different from that of bare CNFs[42] due to the coexistence of γ-Fe_2O_3. The effect of CNFs could also be observed in the charging process. During the first anodic scan, the peak around 1.00 V demonstrated the reaction of the extraction of Li^+ from CNFs. The other two peaks at 1.62 and 1.81 V corresponded to the re-forming of Fe_2O_3 through the oxidation of Fe^0 to Fe^{2+} and Fe^{3+}. As the reversible oxidation reactions were reflected in Figure 6a, a smooth voltage increase up to 0.83 V was observed and the increase rate was slower until ~1.5 V, which was then followed by a further sloping voltage plateau to ~2.0 V and a steep rise up to 3.0 V. The first charge capacity is 1102 mAh g^{-1}, and therefore, the initial capacity loss during the first cycle is 36%. The high ICL value in comparison with commercialized graphite product is well-known due to the extra consumption of Li for the formation of SEI under deep discharge conditions.[40,43,44] Similar ICL was noted with other metal oxides or metal oxide combinations reported in previous literature.[38,45−50]

From the second cycle onward, the cathodic peaks at 1.21 and 0.91 V disappeared, indicating the irreversibility of lithium insertion and phase transformation, as described in eqs 1 and 2. Still, a large amount of lithium could be reversibly cycled in iron oxides by the conversion reaction of eq 3 and CNFs by the intercalation reaction of eq 4. Split peaks observed at 0.84 and 0.97 V in the second discharge transformed to one large peak in further reduction cycles. Correspondingly, as demonstrated in Figure 6a, the second discharge capacity was found to be 1100 (±5) mAh g^{-1}, whereas the value was 1064 and 1027 mAh g^{-1} for the third and fifth cycles, respectively. On the other hand, anodic peaks in the later scans after the first cycle slightly shifted to higher potentials, which indicate the "conditioning" of the electrode in the first few cycles. Such a process undergoes minor structural rearrangement of the active materials and enables good electrical contact among cell components, which are beneficial for the cell stability during further cycling.[51] For the charge curves, no obvious plateaus could be observed.

To compare with γ-Fe_2O_3@CNF, the charge−discharge curve for α-Fe_2O_3 NP is also presented in Figure 6b. The galvanostatic profile of α-Fe_2O_3 NP follows the electrochemical characteristics of nano α-Fe_2O_3, as the first discharge curve contains a monophasic process for Fe_2O_3 up to 1 Li uptake per formula unit, followed by a biphasic transformation.[31] Thus, the initial discharge capacity of α-Fe_2O_3 NP observed could reach as high as 1456 mAh g^{-1}. However, the capacity decreased very fast in the next few cycles, which is due to the formation of nanoaggregates for α-Fe_2O_3 NPs. In comparison with γ-Fe_2O_3@CNF, the voltage plateau of the α-Fe_2O_3 NP between 0.9 and 1.0 V shrank quickly from the second cycle onward, leading to a 72.5% decrease at the end of the fifth cycle. The large differences of galvanostatic profiles are in contrast with the similarity of CV curves between the two samples. The cyclic

dx.doi.org/10.1021/am404939q | ACS Appl. Mater. Interfaces 2014, 6, 1951−1958

voltammograms found for α-Fe_2O_3 previously[31−34] and here (Figure S3, Supporting Information) are quite similar, except for some minor shift on certain peak voltages possibly due to the integrated effects of CNF and iron oxides. This indicates that the reaction mechanisms for iron oxides with different phases are mostly the same, and their differences in electrochemical performances are largely affected by their morphologies.

Figure 7 shows charge and discharge capacities as well as Coulombic efficiency as a function of cycle number of γ-Fe_2O_3@CNF at a current density of 50 mA g^{-1} at room temperature. The discharge capacities of α-Fe_2O_3 NP and CNF-600 (bare electrospun CNF fabricated under carbonization temperature of 600 °C for 12 h) are also presented for comparison. It is obvious that γ-Fe_2O_3@CNF demonstrates much higher reversible capacity and better cyclic stability than both α-Fe_2O_3 NP and bare CNF. After 40 cycles, the capacity observed is about 837 mAh g^{-1} with ∼76% retention of the first reversible capacity, which is 3-fold more than that achieved from α-Fe_2O_3 NP and bare CNF. The overall enhanced electrochemical performance is attributed to the 1D nanostructure induced by electrospun CNF and well-controlled distribution of Fe_2O_3 nanoparticles on the fiber surface, which can buffer the volumetric change during cycling, shorten the diffusion pathways for electronic and lithium ions, and facilitate the reversible decomposition of the Li_2O matrix. The Coulombic efficiency for γ-Fe_2O_3@CNF is also found to be considerably high (>97%) for most cycles despite the high capacity loss during the first cycle, which is widely reported for transition-metal oxides.[52−54] Moreover, differences in the capacity retention regarding iron oxides are noted depending on the method of preparation and reaction conditions.[32,55]

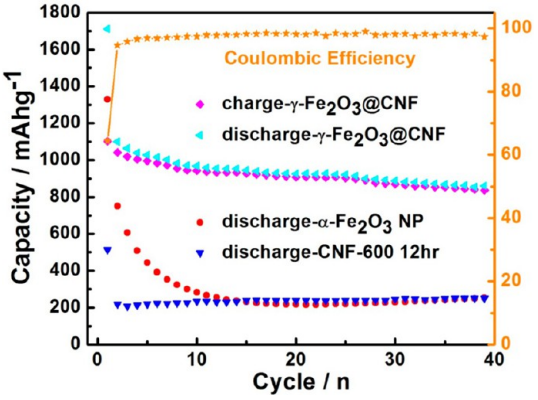

Figure 7. Charge and discharge capacities with Coulombic efficiency as a function of cycle number of γ-Fe_2O_3@CNF, α-Fe_2O_3 NP, and CNF-600 at a current density of 50 mA g^{-1} at room temperature.

The rate capacity test was also carried out on a duplicate cell with γ-Fe_2O_3@CNF in the voltage range of 0.005−3.0 V at different current rates of 0.1, 0.2, 0.5, 1, 2, and 5 A g^{-1}. Results are shown in Figure 8. In Figure 8a, the results of α-Fe_2O_3 NP and CNF-600 are presented for comparison. The observed capacity of 910 mAh g^{-1} after 15 cycles at 0.1 A g^{-1} drops to ∼800 mAh g^{-1} at 0.2 A g^{-1}. The capacity value decreases further at higher rates at 0.5, 1, 2, and 5 A g^{-1}, and a capacity of 336 mAh g^{-1}, comparable to that of graphite, is still obtained at 5 A g^{-1}. After 65 cycles, when the current rate is reduced back to 0.1 A g^{-1}, a reversible capacity of 900 mAh g^{-1} is obtained, showing the good rate capability of the material. The

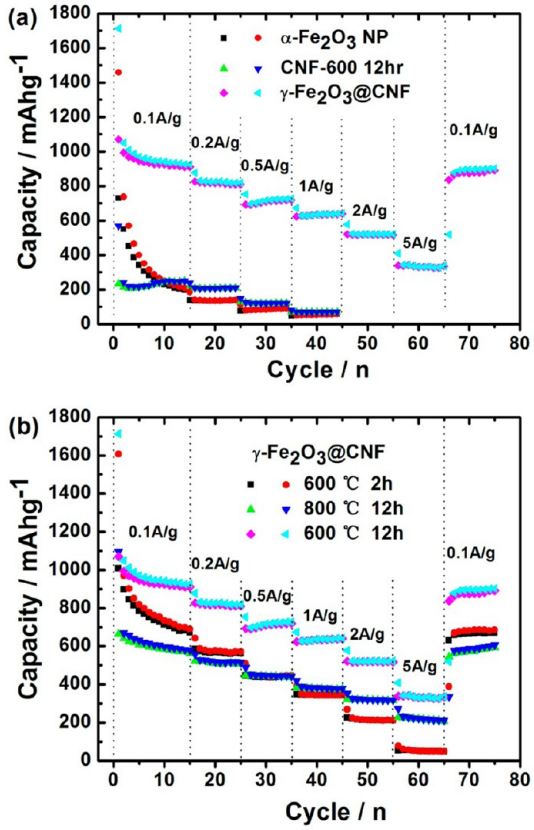

Figure 8. Cycling performance at various current densities (from 0.1, 0.2, 0.5, 1, 2, 5 A g^{-1}) for (a) γ-Fe_2O_3@CNF, α-Fe_2O_3 NP, and CNF-600; and (b) γ-Fe_2O_3@CNF carbonized under different carbonization conditions (600 °C for 12 h, 600 °C for 2 h, and 800 °C for 12 h).

sustainability of γ-Fe_2O_3@CNF at high current density makes the material applicable in the high-power LIBs. In contrast, the α-Fe_2O_3 NP and CNF-600 are exhibiting very low capacity when the current rate increases to 1 A g^{-1}. A reversible capacity ∼ 60 mAh g^{-1} can only be achieved by these two individual components.

Figure 8b demonstrates the rate capacity of γ-Fe_2O_3@CNF carbonized under different carbonization conditions (600 °C for 12 h, 600 °C for 2 h, and 800 °C for 12 h). The variation of current rate applied is the same as that in Figure 8a. γ-Fe_2O_3@CNF carbonized at 600 °C for 12 h presents the highest capacity at all current rates among the three samples. This can be expected from the well-controlled morphology via tuning the fabrication condition as discussed above. The sample carbonized at 600 °C for 2 h demonstrates the fastest capacity loss at higher current rates, which is due to the insufficient conductivity of as-prepared CNFs under that condition. Although the sample carbonized at 800 °C for 12 h showed good capacity retention at increasing current rates, its overall capacity value is much lower than the batch carbonized at 600 °C for 12 h. The result once more confirms that carbonization condition can be optimized at 600 °C for 12 h because of the well-controlled morphology of as-prepared γ-Fe_2O_3@CNF delivering an optimal performance regarding both power and energy density. This is consistent with the electrochemical impedance studies (EIS) that are shown in Figure S4 (Supporting Information), where the 1D nanostructure γ-Fe_2O_3@CNF (600 °C for 12 h) has the lowest impedance after cycling. The smallest semicircle of γ-Fe_2O_3@CNF in EIS

representing the lowest overall impedance value is the indication of its good electrode kinetics.

CONCLUSION

In summary, γ-Fe_2O_3@CNF was synthesized via a hybrid synthesis combining the electrospinning technique and hydrothermal method. The optimized carbonization condition at 600 °C for 12 h helps to form a well-controlled distribution of γ-Fe_2O_3 nanoparticles on 1D CNFs, leading to better electrochemical performance. The as-optimized integrated γ-Fe_2O_3@CNF demonstrated much higher reversible capacity, good cycling, and a rate behavior in comparison with separate components (Fe_2O_3 NPs and bare CNF). The greatly improved electrochemical performance can be attributed to the 1D nanostructure induced by the electrospinning technique that can buffer the volumetric change during cycling, shorten the diffusion pathways for electronic and lithium ions, and facilitate the reversible decomposition of Li_2O. Moreover, the sustainability of γ-Fe_2O_3@CNF at a high current density up to 5 A g^{-1} can be achieved. We believe that our strategy of incorporating high-energy materials on 1D electrospun CNFs can be extended to synthesize other prospective high-power anode materials for LIBs.

ASSOCIATED CONTENT

Supporting Information

SEM comparison of C-γ-Fe_2O_3 carbonized at 600 °C for 2 h and 800 °C for 12 h, XRD patterns of γ-Fe_2O_3@CNF carbonized under different carbonization conditions, cyclic voltammogram of α-Fe_2O_3, and impedance spectroscopy studies are shown for comparison. This material is available free of charge via the Internet at http://pubs.acs.org.

AUTHOR INFORMATION

Corresponding Author

*E-mail: phymvvr@nus.edu.sg, msemvvr@nus.edu.sg, reddymvvr@gmail.com. Fax: + 65-67776126. Tel: + 65-65162607.

Notes

The authors declare no competing financial interest.

ACKNOWLEDGMENTS

Mr. Wu appreciates the scholarship provided by NUS Graduate School for Integrative Sciences and Engineering for his Ph.D. study.

REFERENCES

(1) Armand, M.; Tarascon, J. M. *Nature* **2008**, *451*, 652−657.
(2) Girishkumar, G.; McCloskey, B.; Luntz, A. C.; Swanson, S.; Wilcke, W. *J. Phys. Chem. Lett.* **2010**, *1*, 2193−2203.
(3) Bruce, P. G.; Scrosati, B.; Tarascon, J. M. *Angew. Chem., Int. Ed.* **2008**, *47*, 2930−2946.
(4) Guo, Y. G.; Hu, J. S.; Wan, L. J. *Adv. Mater.* **2008**, *20*, 2878−2887.
(5) Dunn, B.; Kamath, H.; Tarascon, J. M. *Science* **2011**, *334*, 928−935.
(6) Daniel, C., Besenhard, J. O., Eds. *Handbook of Battery Materials*, 2nd ed.; Wiley-VCH Verlag GmbH & Co. KGaA: Weinheim, Germany, 2011.
(7) Reddy, M. V.; Subba Rao, G. V.; Chowdari, B. V. R. *Chem. Rev.* **2013**, *113*, 5364−5457.
(8) Jiang, J. A.; Li, Y. Y.; Liu, J. P.; Huang, X. T. *Nanoscale* **2011**, *3*, 45−58.
(9) Wu, Y. Z.; Chowdari, B. V. R.; Ramakrishna, S. *Curr. Org. Chem.* **2013**, *17*, 1411−1423.
(10) Agend, F.; Naderi, N.; Fareghi-Alamdari, R. *J. Appl. Polym. Sci.* **2007**, *106*, 255−259.
(11) Kim, C.; Yang, K. S.; Kojima, M.; Yoshida, K.; Kim, Y. J.; Kim, Y. A.; Endo, M. *Adv. Funct. Mater.* **2006**, *16*, 2393−2397.
(12) Bonino, C. A.; Ji, L. W.; Lin, Z.; Toprakci, O.; Zhang, X. W.; Khan, S. A. *ACS Appl. Mater. Interfaces* **2011**, *3*, 2534−2542.
(13) Huang, Z. M.; Zhang, Y. Z.; Kotaki, M.; Ramakrishna, S. *Compos. Sci. Technol.* **2003**, *63*, 2223−2253.
(14) Li, D.; Babel, A.; Jenekhe, S. A.; Xia, Y. N. *Adv. Mater.* **2004**, *16*, 2062−2066.
(15) Kumar, P. S.; Sahay, R.; Aravindan, V.; Sundaramurthy, J.; Ling, W. C.; Thavasi, V.; Mhaisalkar, S. G.; Madhavi, S.; Ramakrishna, S. *J. Phys. D: Appl. Phys.* **2012**, *45*, 265302.
(16) Lee, B. S.; Son, S. B.; Park, K. M.; Yu, W. R.; Oh, K. H.; Lee, S. H. *J. Power Sources* **2012**, *199*, 53−60.
(17) Ji, L. W.; Toprakci, O.; Alcoutlabi, M.; Yao, Y. F.; Li, Y.; Zhang, S.; Guo, B. K.; Lin, Z.; Zhang, X. W. *ACS Appl. Mater. Interfaces* **2012**, *4*, 2672−2679.
(18) Wu, Y. Z.; Balakrishna, R.; Reddy, M. V.; Nair, A. S.; Chowdari, B. V. R.; Ramakrishna, S. *J. Alloys Compd.* **2012**, *517*, 69−74.
(19) Binitha, G.; Soumya, M. S.; Madhavan, A. A.; Praveen, P.; Balakrishnan, A.; Subramanian, K. R. V.; Reddy, M. V.; Nair, S. V.; Nair, A. S.; Sivakumar, N. *J. Mater. Chem. A* **2013**, *1*, 11698−11704.
(20) Wang, H. G.; Ma, D. L.; Huang, X. L.; Huang, Y.; Zhang, X. B. *Sci. Rep.* **2012**, *2*, 701.
(21) Das, B.; Reddy, M. V.; Chowdari, B. V. R. *Nanoscale* **2013**, *5*, 1961−1966.
(22) Wu, Y. Z.; Zhu, P. N.; Zhao, X.; Reddy, M. V.; Peng, S. J.; Chowdari, B. V. R.; Ramakrishna, S. *J. Mater. Chem. A* **2013**, *1*, 852−859.
(23) Wang, X.; Chen, X. Y.; Gao, L. S.; Zheng, H. G.; Ji, M. R.; Tang, C. M.; Shen, T.; Zhang, Z. D. *J. Mater. Chem.* **2004**, *14*, 905−907.
(24) Chen, Y.; Zhu, C. L.; Shi, X. L.; Cao, M. S.; Jin, H. B. *Nanotechnology* **2008**, *19*, 205603.
(25) Ji, L. W.; Lin, Z.; Medford, A. J.; Zhang, X. W. *Chem.—Eur. J.* **2009**, *15*, 10718−10722.
(26) Hariharan, S.; Saravanan, K.; Balaya, P. *Electrochem. Solid-State Lett.* **2010**, *13*, A132−A134.
(27) Wu, Y.; Reddy, M. V.; Chowdari, B. V. R.; Ramakrishna, S. *ACS Appl. Mater. Interfaces* **2013**, *5*, 12175−12184.
(28) Inagaki, M.; Yang, Y.; Kang, F. *Adv. Mater.* **2012**, *24*, 2547−2566.
(29) Wang, Y.; Santiago-Aviles, J. J.; Furlan, R.; Ramos, I. *IEEE Trans. Nanotechnol.* **2003**, *2*, 39−43.
(30) Shafi, K. V. P. M.; Ulman, A.; Dyal, A.; Yan, X. Z.; Yang, N. L.; Estournes, C.; Fournes, L.; Wattiaux, A.; White, H.; Rafailovich, M. *Chem. Mater.* **2002**, *14*, 1778−1787.
(31) Larcher, D.; Bonnin, D.; Cortes, R.; Rivals, I.; Personnaz, L.; Tarascon, J. M. *J. Electrochem. Soc.* **2003**, *150*, A1643−A1650.
(32) Reddy, M. V.; Yu, T.; Sow, C. H.; Shen, Z. X.; Lim, C. T.; Subba Rao, G. V.; Chowdari, B. V. R. *Adv. Funct. Mater.* **2007**, *17*, 2792−2799.
(33) Cherian, C. T.; Sundaramurthy, J.; Kalaivani, M.; Ragupathy, P.; Kumar, P. S.; Thavasi, V.; Reddy, M. V.; Sow, C. H.; Mhaisalkar, S. G.; Ramakrishna, S.; Chowdari, B. V. R. *J. Mater. Chem.* **2012**, *22*, 12198−12204.
(34) Chaudhari, S.; Srinivasan, M. *J. Mater. Chem.* **2012**, *22*, 23049−23056.
(35) Larcher, D.; Masquelier, C.; Bonnin, D.; Chabre, Y.; Masson, V.; Leriche, J. B.; Tarascon, J. M. *J. Electrochem. Soc.* **2003**, *150*, A133−A139.
(36) Jamnik, J.; Maier, J. *Phys. Chem. Chem. Phys.* **2003**, *5*, 5215−5220.
(37) Shin, J. Y.; Samuelis, D.; Maier, J. *Adv. Funct. Mater.* **2011**, *21*, 3464−3472.
(38) Reddy, M. V.; Wei Wen, B. L.; Loh, K. P.; Chowdari, B. V. R. *ACS Appl. Mater. Interfaces* **2013**, *5*, 7777−7785.

(39) Reddy, M. V.; Prithvi, G.; Loh, K. P.; Chowdari, B. V. R. *ACS Appl. Mater. Interfaces* **2013**, DOI: 10.1021/am4047552.
(40) Laruelle, S.; Grugeon, S.; Poizot, P.; Dolle, M.; Dupont, L.; Tarascon, J. M. *J. Electrochem. Soc.* **2002**, *149*, A627−A634.
(41) Debart, A.; Dupont, L.; Poizot, P.; Leriche, J. B.; Tarascon, J. M. *J. Electrochem. Soc.* **2001**, *148*, A1266−A1274.
(42) Wu, Y. Z.; Reddy, M. V.; Chowdari, B. V. R.; Ramakrishna, S. *ACS Appl. Mater. Interfaces* **2013**, *5*, 12175−12184.
(43) Poizot, P.; Laruelle, S.; Grugeon, S.; Dupont, L.; Tarascon, J. M. *Nature* **2000**, *407*, 496−498.
(44) Sharma, Y.; Sharma, N.; Subba Rao, G. V.; Chowdari, B. V. R. *Adv. Funct. Mater.* **2007**, *17*, 2855−2861.
(45) Cherian, C. T.; Reddy, M. V.; Haur, S. C.; Chowdari, B. V. R. *ACS Appl. Mater. Interfaces* **2013**, *5*, 918−923.
(46) Cherian, C. T.; Zheng, M. R.; Reddy, M. V.; Chowdari, B. V. R.; Sow, C. H. *ACS Appl. Mater. Interfaces* **2013**, *5*, 6054−6060.
(47) Reddy, M. V.; Yu, C.; Fan, J. H.; Loh, K. P.; Chowdari, B. V. R. *ACS Appl. Mater. Interfaces* **2013**, *5*, 4361−4366.
(48) Cherian, C. T.; Sundaramurthy, J.; Reddy, M. V.; Suresh Kumar, P.; Mani, K.; Pliszka, D.; Sow, C. H.; Ramakrishna, S.; Chowdari, B. V. R. *ACS Appl. Mater. Interfaces* **2013**, *5*, 9957−9963.
(49) Tao, T.; Glushenkov, A. M.; Zhang, C. F.; Zhang, H. Z.; Zhou, D.; Guo, Z. P.; Liu, H. K.; Chen, Q. Y.; Hu, H. P.; Chen, Y. *J. Mater. Chem.* **2011**, *21*, 9350−9355.
(50) Rahman, M. M.; Glushenkov, A. M.; Ramireddy, T.; Tao, T.; Chen, Y. *Nanoscale* **2013**, *5*, 4910−4916.
(51) Reddy, M. V.; Subba Rao, G. V.; Chowdari, B. V. R. *J. Power Sources* **2010**, *195*, 5768−5774.
(52) Morimoto, H.; Tobishima, S.; Iizuka, Y. *J. Power Sources* **2005**, *146*, 315−318.
(53) Hang, B. T.; Doi, T.; Okada, S.; Yamaki, J. I. *J. Power Sources* **2007**, *174*, 493−500.
(54) Liu, S. L.; Zhang, L. N.; Zhou, J. P.; Xiang, J. F.; Sun, J. T.; Guan, J. G. *Chem. Mater.* **2008**, *20*, 3623−3628.
(55) Reddy, M. V.; Cherian, C. T.; Ramanathan, K.; Jie, K. C. W.; Daryl, T. Y. W.; Hao, T. Y.; Adams, S.; Loh, K. P.; Chowdari, B. V. R. *Electrochim. Acta* **2014**, *118*, 75−80.